

Fast Continuous Haar and Fourier Transforms of Rectilinear Polygons from VLSI Layouts

Robin Scheibler, *Member, IEEE*, Paul Hurley, *Senior Member, IEEE*, Amina Chebira *Member, IEEE*

Abstract—We develop the pruned continuous Haar transform and the fast continuous Fourier series, two fast and efficient algorithms for rectilinear polygons. Rectilinear polygons are used in VLSI processes to describe design and mask layouts of integrated circuits. The Fourier representation is at the heart of many of these processes and the Haar transform is expected to play a major role in techniques envisioned to speed up VLSI design. To ensure correct printing of the constantly shrinking transistors and simultaneously handle their increasingly large number, ever more computationally intensive techniques are needed. Therefore, efficient algorithms for the Haar and Fourier transforms are vital.

We derive the complexity of both algorithms and compare it to that of discrete transforms traditionally used in VLSI. We find a significant reduction in complexity when the number of vertices of the polygons is small, as is the case in VLSI layouts. This analysis is completed by an implementation and a benchmark of the continuous algorithms and their discrete counterpart. We show that on tested VLSI layouts the pruned continuous Haar transform is 5 to 25 times faster, while the fast continuous Fourier series is 1.5 to 3 times faster.

Index Terms—Continuous transform, Fast Haar and Fourier algorithms, 2D rectilinear polygons, VLSI

I. INTRODUCTION

MOORE'S famous law from 1965 [1] has been a major driving force in the effort to shrink transistors in Very Large Scale Integration (VLSI). The tremendous progress in optical lithography has been the enabler for massive production of integrated circuits and a dramatic decrease in unit cost.

In optical lithography [2], patterns of the integrated circuits are transferred to silicon by shining light through a mask and subsequently using a lens to concentrate the light onto a photosensitive layer, as depicted in Fig. 1. This is followed by an etching step, which transfers the pattern to the silicon. The Fourier transform of the mask is extensively used in simulation of the lithography process owing to Fourier transforming properties of lenses [3]. The projected image is the convolution of the mask with an ideal filter with frequency response $H(f, g) = 1$ if $\sqrt{f^2 + g^2} \leq \frac{NA}{\lambda}$ and 0 otherwise, where f and g are the spatial frequencies, NA the numerical aperture of the lens and λ the wavelength of the source [4]. The size of the smallest feature printable by straightforward means with such a lithography system is $0.25\lambda/NA$ [5].

R. Scheibler and P. Hurley are with the System Software group at IBM Research – Zürich, Säumerstrasse 4, 8803 Rüschlikon, Switzerland (robin.scheibler@ieee.org and pah@zurich.ibm.com).

A. Chebira is with the Audiovisual Communications Laboratory (LCAV), School of Computer & Communication Sciences, École Polytechnique Fédérale de Lausanne (EPFL), 1015 Lausanne, Switzerland (amina.chebira@epfl.ch).

The smallest feature in integrated circuits, also called technology node, has shrunk from a few micrometers in the early days of optical lithography to 32nm for the latest commercially available technology. The next industry target is to print 22nm with sufficient yield. One way to achieve this target is to develop extreme ultra-violet light source [6], which, with a wavelength of 15nm, would enable reliable production of future technology nodes. However, it will seemingly not be ready on time for the 22nm node, and remains to be proved a viable technology. This means the current state of the art light source with a wavelength of 193nm has to be used for the 22nm node. Along with a numerical aperture of $NA = 1.44$ in modern lithography systems, this sets the smallest feature possible at 34nm.

For the 32nm technology node, the system has already been pushed past its apparent limit. At 22nm, the system is operating far below its limit, resulting in severe optical degradation due to printed shapes being much smaller than allowed by the current wavelength of the light. As a consequence, ever more burden is placed onto computationally intensive techniques to circumvent the optical degradation, and thus ensure sufficient manufacturing yield. These techniques, collectively known as *computational lithography*, include traditional resolution enhancement [4], source-mask optimization [7], and inverse lithography [8]. They strive to exploit all degrees of freedom in the lithography process, including illumination amplitude, direction and phase [5]. All of these techniques rely on computationally intensive simulation of the underlying physical processes. An alternative is to replace the simulation altogether by a statistical model. For example, Kryszczuk et al. [9] avoid costly physical simulation by directly predicting the printability of the layouts using a classifier trained with feature vectors from orthogonal transforms.

VLSI layout file sizes are expanding rapidly, with an increasing number of transistors packed into a single design. They can reach more than a terabyte for a single layer in technology nodes under 40nm [10]. This coincides unfortunately with the increasing complexity of the aforementioned computational lithography algorithms. Taking these factors into account, having highly efficient algorithms at various steps of the lithography process becomes crucial.

VLSI layouts consist primarily of highly repetitive patterns of rectilinear polygons, those containing only right angles. Their vertex description, although very compact, is cumbersome to use for applications where a fixed-length representation is required, in particular machine learning. However, they are also very sparse in the Haar basis since the building blocks of its basis functions are themselves rectangles. The

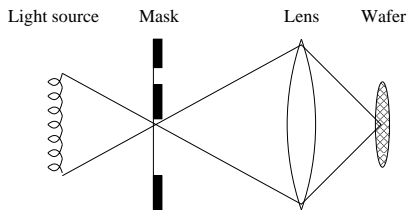


Fig. 1. Basic principle of optical lithography. Patterns of the integrated circuit are transferred to the silicon wafer by shining light through a mask and subsequently using a lens to concentrate the light onto a photosensitive layer.

Haar transform is thus a potentially excellent candidate to provide fixed-length features for any post-processing envisioned in computational lithography. To extract Haar transform coefficients from such enormous amount of vertex descriptions of polygons, one needs a fast algorithm.

The Fourier representation is crucial in computational lithography, especially in simulation of the lithography process. The underlying physical processes is continuous, and using the continuous Fourier series (CFS) would seem natural. However, a discretization step, comprising the sampling of the polygons, followed by a fast Fourier transform is instead standard practice. Unfortunately, sampling introduces aliasing and thus reduces overall accuracy. CFS does not suffer from aliasing. However, a fast and efficient algorithm is required to make the use of CFS practical given the extreme amount of data to process in VLSI layouts.

Despite its close affinity with rectilinear polygons, the Haar transform has seen surprisingly little use in lithography-related algorithms. In 1985, Haslam et al. used a discrete Haar transform to compress the Fourier precompensation filters for electron-beam lithography [11], whereas Ma et al. used the Haar transform in inverse lithography to regularize the obtained mask [12]. When only a sampled signal is available, a continuous transform cannot be computed. Even the so-called continuous wavelet transform is computed as the projection of a discrete signal onto an overcomplete basis [13]. For polygons it is however possible to compute the inner products with continuous basis functions. In [14], we introduced the pruned continuous Haar transform (PCHT), a fast algorithm to compute the continuous Haar transform coefficients. We further study this algorithm in more detail in this paper.

As mentioned, the Fourier transform is extensively used at various levels of the lithography process. Uses of the fast Fourier transform (FFT) include the computation of a precompensation filter to reduce proximity effects [15], and approximating the diffraction orders of the mask [7]. In [16], a road map for the efficient use of the 2D FFT in computational lithography is developed. The mathematical idea to compute the CFS of polygons in itself is not new. In 1983, Lee and Mitra used geometry to derive a closed-form expression for the Fourier integral over a polygon [17]. A few years later, Chu and Huang proposed a new and elegant derivation based on Stokes' theorem [18]. More recently, both Brandoli et al. [19] and Lu et al. [20] extended the solutions to the N -dimensional case using the divergence theorem.

The inherently continuous nature of polygons makes a

continuous transform a natural tool for VLSI layouts. To the best of our knowledge, algorithms making efficient use of this type of representation to quickly compute continuous transform coefficients do not exist. We present in this paper the first fast and efficient continuous Haar transform and Fourier series algorithms applied to rectilinear polygons from VLSI layouts. They are based on a closed-form formula that we derive for 2D continuous separable transforms using a decomposition of rectilinear polygons into rectangles. This formulation allows us to derive two fast algorithms to compute the transform coefficients: PCHT, first introduced in [14], and the fast continuous Fourier series (FCFS) algorithms. PCHT has a fast orthogonal wavelet transform structure that is pruned using computational geometry techniques. FCFS results from reducing the CFS computation problem to a few sparse discrete Fourier transforms (DFT) computed using pruned FFT algorithms. We evaluate the complexity of both algorithms and the performance of their implementation on real VLSI layouts relative to their discrete counterparts. We find PCHT and FCFS to be up to 25 and 3 times, respectively, faster than their discrete counterparts.

This paper is organized as follows. Section II introduces the necessary background in VLSI layouts, the continuous Haar transform (CHT), and the CFS. Section III presents a framework for taking continuous transforms of rectilinear polygons as well as the proposed PCHT and FCFS. In Section IV, the performance of both algorithms is evaluated and compared to that of their discrete counterparts. Finally, Section V concludes by discussing the superiority of PCHT and FCFS over their discrete equivalents, and sketches possible future directions.

II. BACKGROUND

In this section, we first briefly describe VLSI layouts and how they are created. The rectilinear polygons composing VLSI layouts are described mathematically, laying the groundwork for the algorithms to come. We then describe the 2D continuous Haar transform and the fast wavelet transform algorithm used to compute it. Finally, a short refresher on the CFS is given.

A. VLSI Layouts

1) *Layouts*: VLSI layouts are composed of millions of rectangles, or more generally, rectilinear polygons, which come from the transformation of elements of a functional electric circuit. This data is then used for tasks such as mask generation and printing using an optical lithography system.

Such a layout typically consists of several layers of various types. Fig. 2 shows fragments of three different types of layers. These are taken from Metal 1 (M1), which is mostly random logic, Metal 2 (M2), containing some logic and wires and Contact Array (CA), providing contacts between the different layers. In addition, there are several other types of layers, omitted here, similar to those of M1, M2 or CA.

2) *Rectilinear Polygons*: We now give a mathematical definition of the polygons in VLSI layouts. They are rectilinear (only right angles), simple (edges do not intersect, no

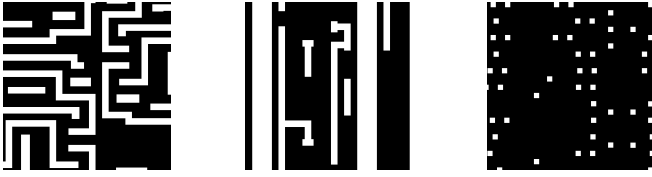


Fig. 2. From left to right: Examples of 1024nm×1024nm tiles from Metal 1, Metal 2 and Contact Array layers, respectively. Note that they exclusively contain rectilinear polygons.

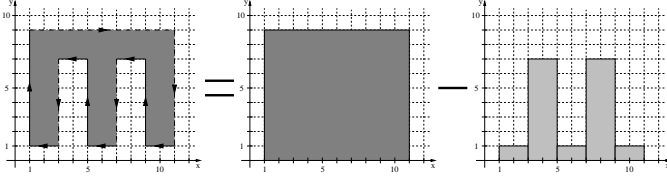


Fig. 3. On the left, a rectilinear simple lattice polygon. The interior of the polygon is shaded. The full-lined edges are included, while the dashed edges are not. Arrows indicate vertex ordering. On the right, illustration of the construction of the left polygon from disjoint rectangles. The minus here stands for the set difference operator.

holes), lattice (vertices are on the integer lattice) polygons. An example of such a polygon is shown in Fig. 3.

A standard layout description consists of polygons defined by the set of the ordered coordinates of their K vertices

$$\{(x_0, y_0), \dots, (x_{K-1}, y_{K-1})\}, \quad (x_i, y_i) \in \mathbb{Z}^2. \quad (1)$$

This set separates the plane in two: inside and outside of the polygon. A sequence order is also needed, which we arbitrarily choose to be clockwise. A disjoint partition of the plane is achieved when we exclude edges if the interior of the polygon is on their left or bottom and include them if the interior is on the right or top (see Fig. 3).

Rectangles are rectilinear polygons with four vertices, and as they are simpler to handle, we treat them as a special case. A rectangle \mathcal{R} can be defined by its lower left and upper right vertices

$$\mathcal{R}_{(x_1, y_1)}^{(x_2, y_2)} = \{(x, y) \mid x_1 \leq x < x_2, y_1 \leq y < y_2\}.$$

The following result, illustrated in Fig. 3, makes it easy to take inner products over rectilinear polygons.

Proposition 1: Any rectilinear polygon \mathcal{P} with K vertices as in (1) can be expressed by $K/2$ disjoint rectangles, each with a side lying on the x -axis

$$\mathcal{P} = \bigcup_{\{i \mid x_{i+1} > x_i\}} \mathcal{R}_{(x_i, 0)}^{(x_{i+1}, y_i)} \setminus \bigcup_{\{i \mid x_{i+1} < x_i\}} \mathcal{R}_{(x_{i+1}, 0)}^{(x_i, y_i)} \quad (2)$$

where the indices are taken modulo K and \setminus is the set difference operator.

An equivalent result exists for the case where a side is lying on the y -axis.

So far polygons have been defined as subsets of \mathbb{R}^2 , and are not yet directly transformable as 2D signals on \mathbb{R}^2 . This is achieved by transforming their indicator function

$$f_{\mathcal{P}}(x, y) = \mathbb{1}_{\mathcal{P}}(x, y)$$

where $\mathcal{P} \subset \mathbb{R}^2$ is the polygon and $\mathbb{1}_{\mathcal{S}}(x, y) = 1$, if $(x, y) \in \mathcal{S}$ and 0 otherwise, is the indicator function of a set \mathcal{S} .

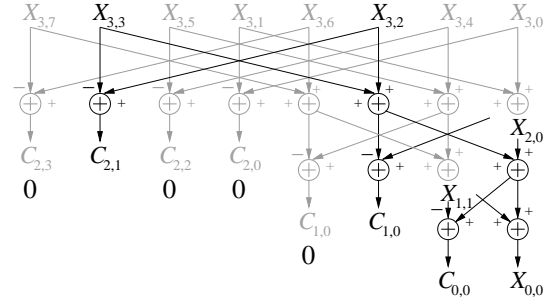


Fig. 4. A pruned signal flow of the 1D Haar FWT. The full flow-diagram is shown in light gray. The transformed signal is $f(t) = u(t-3)$, defined on $[0, 8)$, where $u(t)$ is the Heaviside function. $X_{j,k} = \langle f, \varphi_{j,k}^{(8)} \rangle$ and $C_{j,k} = \langle f, \psi_{j,k}^{(8)} \rangle \cdot \varphi_{j,k}^{(8)}$ and $\psi_{j,k}^{(8)}$ are the 1D Haar basis functions on $[0, 8)$. For simplicity, the scaling of the transform coefficients has been omitted.

B. Continuous Haar Transform

The 2D Haar basis over $\mathbf{T} = [0, N_x) \times [0, N_y)$ is

$$\left\{ \varphi_{0,0,0}, \psi_{j,k_x,k_y}^{(hg)}, \psi_{j,k_x,k_y}^{(gh)}, \psi_{j,k_x,k_y}^{(hh)} \right\} \quad (3)$$

where $j \in \mathbb{N}$ and $k_x, k_y \in \{0, \dots, 2^j - 1\}$. In practice, j is limited to some maximum level of decomposition J . The scaling function is

$$\varphi_{j,k_x,k_y}(x, y) = \frac{2^j}{\sqrt{N_x N_y}} \varphi\left(\frac{2^j}{N_x} x - k_x\right) \varphi\left(\frac{2^j}{N_y} y - k_y\right)$$

where $\varphi(t) = 1$ if $0 \leq t < 1$ and 0 otherwise. The three other basis functions can be defined using a recursive relationship. For example

$$\psi_{j,k_x,k_y}^{(hg)}(x, y) = \sum_n \sum_m h_n g_m \varphi_{j+1, 2k_x+n, 2k_y+m}(x, y)$$

where $g_n = [2^{-1/2} 2^{-1/2}]$ and $h_n = [2^{-1/2} - 2^{-1/2}]$ are the Haar filters. By replacing $h_n g_m$ in the sum by $g_n g_m$, $g_n h_m$ and $h_n h_m$ we obtain $\varphi_{j,k_x,k_y}^{(gh)}$ and $\psi_{j,k_x,k_y}^{(hh)}$, respectively. The dyadic CHT of a function f is given by its inner product with the basis functions. The discrete counterpart of the CHT is the discrete Haar transform (DHT). For a more thorough introduction to the CHT and DHT, see [21]. The CHT and DHT coefficients are identical for 2D rectilinear polygonal patterns. Both can be computed using the fast orthogonal wavelet transform (FWT) [22]. This algorithm has a Cooley-Tukey butterfly structure [23], where only the inner products with the scaling function at the lowest level need be computed. The full flow diagram for a length-8 1D FWT is shown in light gray in Fig. 4. Fig. 5 shows one butterfly of the 2D transform.

C. Continuous Fourier Series

The 2D Fourier basis over $\mathbf{T} = [0, N_x) \times [0, N_y)$ is

$$\left\{ (N_x N_y)^{-1/2} e^{j(w_x k_x x + w_y l y)} \right\}_{(k,l) \in \mathbb{Z}^2}, \quad (4)$$

where $w_x = \frac{2\pi}{N_x}$ and $w_y = \frac{2\pi}{N_y}$. The Fourier basis assumes that the function f under transformation is periodic with period N_x along the x -axis and period N_y along the y -axis. The CFS

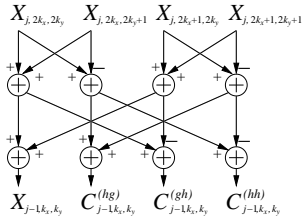


Fig. 5. One butterfly of the traditional 2D Haar FWT where $X_{j,k_x,k_y} = \langle f, \varphi_{j,k_x,k_y} \rangle$ and $C_{j,k_x,k_y}^{(a,b)} = \langle f, \psi_{j,k_x,k_y}^{(ab)} \rangle$, $j \in \mathbb{N}$, $k_x, k_y \in \{0, \dots, 2^j - 1\}$, and $a, b \in \{g, h\}$. Scaling of the transform coefficients is omitted for simplicity.

coefficients $\hat{F}_{k,l}$ are then given by the inner product between f and the Fourier basis functions.

The main difference with the DFT is that the functions are continuous in the spatial domain, and thus not periodic in the frequency domain. This means that for a perfect reconstruction of the image, an infinite number of coefficients is needed. On the other hand, the use of the DFT requires sampling, which in turn introduces aliasing, due to the infinite bandwidth of rectilinear polygons. In contrast, the CFS yields the true spectrum of the continuous image.

III. CONTINUOUS TRANSFORMS OF RECTILINEAR POLYGONS

In this section, we derive the algorithms to compute the continuous Haar transform and Fourier series coefficients of rectilinear polygons. Their theoretical computational complexity is evaluated and compared with that of the equivalent discrete transforms.

The main reason continuous transforms can be faster than their discrete counterparts for rectilinear polygons is that the continuous inner product of a basis function is an explicit function of the vertices of the polygon, and the vertex description (1) is very sparse compared to the size of the image. Moreover, no memory is needed to form or store a discrete image. On the other hand, the sampling of the polygons to create a discrete image can itself be considered a projection on a Dirac basis. Sampling followed by a discrete transform, as illustrated in Fig. 6, effectively is two transforms, whereas a continuous transform can completely omit the sampling operation. Moreover, as discussed in the introduction, sampling introduces aliasing since the assumption that the signal is bandlimited does not hold for rectilinear polygons.

A. Inner Product over Rectilinear Polygons

In practice, layouts are divided into smaller disjoint or overlapping rectangular tiles before applying a transform to each individual tile. Therefore, we consider continuous transforms over a rectangular subset $\mathbf{T} = [0, N_x) \times [0, N_y) \subset \mathbb{R}^2$ that we call a tile. This poses no restrictions as the size can be increased sufficiently to cover the entire layout. In the case of VLSI layouts, N_x, N_y are always chosen to be positive integers. An orthogonal basis of functions $\phi_{k,l}$ over \mathbf{T} can be written as $\{\phi_{k,l} : \mathbf{T} \rightarrow \mathbb{C}\}_{k=0,l=0}^{\infty,\infty}$, and the transform

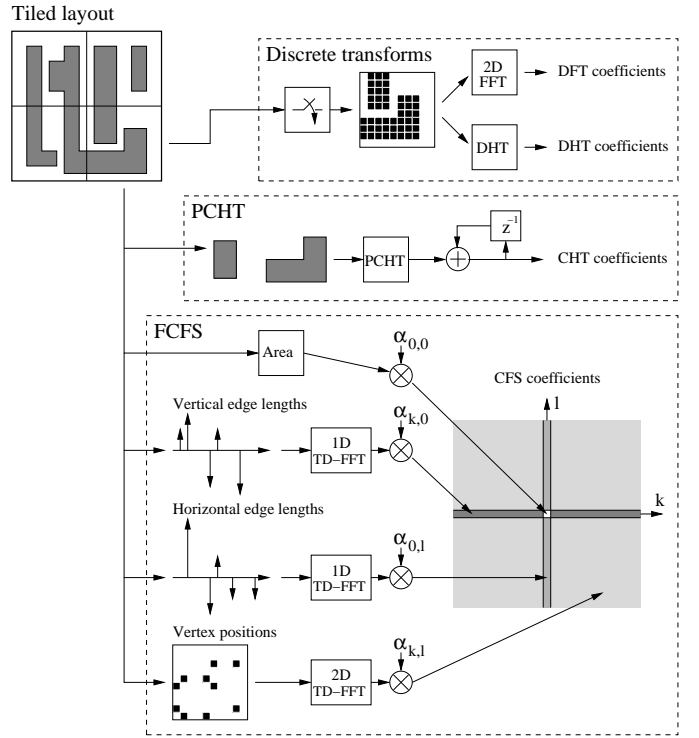


Fig. 6. Flow diagram of all the transforms. From top to bottom: fast Fourier transform (FFT), discrete Haar transform (DHT), pruned continuous Haar transform (PCHT) and fast continuous Fourier series (FCFS).

coefficients of a function $f \in L^2(\mathbf{T})$ are simply the inner products with the basis functions

$$\langle f, \phi_{k,l} \rangle = \iint_{\mathbf{T}} f(x,y) \phi_{k,l}^*(x,y) dx dy. \quad (5)$$

As all polygons in a layout are disjoint, the image $f_{\mathbf{T}}$ of a tile containing polygons $\mathcal{P}_0, \dots, \mathcal{P}_{M-1} \subseteq \mathbf{T}$ is the sum of the indicator functions of the polygons

$$f_{\mathbf{T}}(x,y) = \sum_{m=0}^{M-1} \mathbb{1}_{\mathcal{P}_m}(x,y). \quad (6)$$

Now that we have a signal model, we provide two results that will allow us to derive the inner product of $f_{\mathbf{T}}$ with a given basis function.

Proposition 2: If $f_{\mathbf{T}}(x,y)$ is given by (6) and $\phi_{k,l}(x,y)$ is a basis function, their inner product according to (5) is

$$\langle f_{\mathbf{T}}, \phi_{k,l} \rangle = \sum_{m=0}^{M-1} \sum_{i=0}^{K_m/2-1} \int_0^{y_{m,2i}} \int_{x_{m,2i}}^{x_{m,2i+1}} \phi_{k,l}^*(x,y) dx dy$$

where $(x_{m,i}, y_{m,i})$ is the i^{th} vertex, out of the K_m , of the m^{th} polygon and i is taken modulo K_m . Here it is assumed without loss of generality that for all m $x_{m,0} \neq x_{m,1}$.

Proof: By the linearity of the inner product and since the polygons are disjoint, we have

$$\langle f_{\mathbf{T}}, \phi_{k,l} \rangle = \sum_{m=0}^{M-1} \langle f_{\mathcal{P}_m}, \phi_{k,l} \rangle = \sum_{m=0}^{M-1} \iint_{\mathcal{P}_m} \phi_{k,l}^*(x,y) dx dy. \quad (7)$$

Then, using Proposition 1, we split the integral over \mathcal{P}_m into $K_m/2$ over rectangles. If $x_{m,i} < x_{m,i+1}$, the integral is positive and is added to the final result. If $x_{m,i} > x_{m,i+1}$, the integral is negative and is subtracted from the final result. If $x_{m,i} = x_{m,i+1}$, the i^{th} term of the sum is zero. ■

We now give the closed-form formula for $\langle f_{\mathcal{P}}, \phi_{k,l} \rangle$ when $\phi_{k,l}$ is separable. When there is more than one polygon in the tile, we compute the continuous Haar and Fourier transforms of $f_{\mathcal{T}}$ by simply applying (7). The following lemma is derived using Proposition 2, the separability of $\phi_{k,l}$ and the fact that $\sum_{i=0}^{K/2-1} (\Omega_k^*(x_{2i+1}) - \Omega_k^*(x_{2i})) = 0$ for rectilinear polygons since the index i is cyclic and vertical edges cancel. The function Ω is a primitive of ϕ .

Lemma 1: Consider a rectilinear polygon \mathcal{P} with K vertices, and a separable basis function, namely $\phi_{k,l}(x, y) = \phi_k(x)\phi_l(y)$. Then

$$\langle f_{\mathcal{P}}, \phi_{k,l} \rangle = \sum_{i=0}^{K/2-1} \Omega_l^*(y_{2i}) (\Omega_k^*(x_{2i+1}) - \Omega_k^*(x_{2i})), \quad (8)$$

where indices are taken modulo K .

B. Pruned Continuous Haar Transform (PCHT)

We first describe the PCHT algorithm for rectilinear polygons, first introduced in [14]. We then advance this previous work with the derivation of the complexity of PCHT.

1) *Algorithm Derivation:* Consider the FWT as described in Section II-B and whose full 1D flow diagram is shown in light gray in Fig. 4. First, note that the linear complexity of the FWT and (7) mean that we can use the FWT on individual polygons and sum up the transform coefficients to obtain the transform of a tile, as illustrated in Fig. 6. Thus, from now on, we consider only the transform of a single polygon. Second, we use computational geometry techniques to compute the inner product. The continuous inner product between the indicator of a polygon and the support of the scaling function, as given by Lemma 1, is the area of the geometrical intersection of the polygon and the scaling function multiplied by $2^j/\sqrt{N_x N_y}$. A method to compute the intersection area for rectilinear polygons is described in Algorithm 1.

The Haar transform acts as a discontinuity detector, and all transform coefficients will be zero except when basis functions intersect the boundary of the polygon. Therefore, the basis functions completely inside or outside the polygon can be ignored. In addition, all coefficients positioned below such a basis function in the transform tree are also zero. Fig. 7 shows, in gray, the support of the basis functions of a given scale that yield non-zero inner products. As with the original FWT, PCHT can be written as a divide-and-conquer algorithm: Divide the tile into four rectangular parts recursively until the part under consideration is completely inside or outside the polygon. Pseudocode for PCHT can be found in [14]. An example of the pruned transform flow-diagram for the 1D case is shown in Fig. 4 in black.

2) *Complexity:* We will now estimate the complexity of PCHT. As it is highly dependent on the geometry of the polygon, we make the worst-case assumption and describe the complexity as a function of a few general properties of the

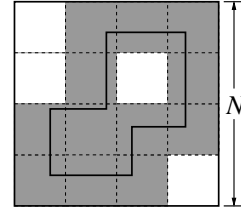


Fig. 7. The Haar basis functions yield zero inner product except when they intersect the edge of a polygon. The big thick square is the tile with $N_x = N_y = N$. The dashed squares are the supports of the basis functions at a given scale. The thick polygonal border marks the contour of the polygon. Basis functions yielding non-zero inner product are shown in gray.

polygon, such as its number of vertices K and its perimeter P . The complexity is also a function of the computational complexity $\Lambda_{ia}(K)$ of the intersection area algorithm. The exact value depends on the assumptions made regarding the type of polygons, but is $O(K)$. In particular, for rectilinear polygons, we have

$$\Lambda_{ia}(K) = \begin{cases} 11 & \text{if } K = 4 \\ 6K - 1 & \text{if } K > 4 \end{cases}, \quad (9)$$

additions, multiplications and comparisons.

We begin by estimating the number of non-terminating recursive calls. A call is non-terminating if the support of the waveform intersects the boundary of the polygon. At a given scale j , there are roughly $\lceil 2^j P/N \rceil$ such basis functions. We assume here that $N_x = N_y = N$. Each of these calls makes four calls to itself and thus to the intersection area routine and also uses three comparisons. The intersection area routine uses in turn eleven additions and three multiplications per non-terminating call. Finally, a total of $M - 1$ additions are needed to sum up the scaling coefficients of the polygons, and a single multiplication is needed for the final scaling factor. We thus formulate our estimate of the complexity of PCHT as

$$\Lambda_{PCHT} \approx \left(\sum_{m=0}^{M-1} \sum_{j=0}^{J-1} \left\lceil \frac{2^j P_m}{N} \right\rceil (\Lambda_{ia}(K_m) + 26) \right) + M \quad (10)$$

operations (additions, multiplications and comparisons), where P_m and K_m are the perimeter and number of vertices of the m^{th} polygon, respectively, M is the number of polygons in a given tile and J the maximum level of decomposition. For a DHT with $N_x = N_y = N = 2^J$, the total number of operations is $\Lambda_{DHT} = \frac{8}{3}(N^2 - 1)$. The relation between the complexity and the actual runtime is discussed in Section IV.

C. Fast Continuous Fourier Series (FCFS)

We now develop the FCFS algorithm for computing the CFS coefficients of rectilinear polygons. The computational complexity of FCFS will also be evaluated and compared with that of the FFT.

1) *Algorithm Derivation:* We begin by a closed-form formula for the CFS coefficients of rectilinear polygons. Applying Lemma 1 to the Fourier basis (4) results in the following proposition.

TABLE I

COMPLEXITY OF THE STEPS OF THE FCFS ALGORITHM. $K = \sum_{m=0}^{M-1} K_m$ IS THE SUM OF THE VERTICES OF THE M POLYGONS IN THE $N_x \times N_y$ TILE. THE PARAMETERS $P_x^{(I)}$, $P_x^{(II)}$, DIVIDERS OF N_x , AND $P_y^{(I)}$, $P_y^{(II)}$, DIVIDERS OF N_y , ARE CHOSEN TO MINIMIZE THE OVERALL COMPLEXITY.

Step	Number of Operations	Operation performed
1	$\frac{3}{2}K - M$	Sum of polygon areas
2	$(\frac{5}{2} + \frac{3}{2}Q_x^{(I)}) \times K + (\frac{1}{2}Q_x^{(I)} + 1) \times C_{FFFT1D}(P_x^{(I)})^\dagger$	1D $\frac{K}{2}$ -input pruned FFT
3	$(\frac{5}{2} + \frac{3}{2}Q_y^{(I)}) \times K + (\frac{1}{2}Q_y^{(I)} + 1) \times C_{FFFT1D}(P_y^{(I)})^\dagger$	1D $\frac{K}{2}$ -input pruned FFT
4	$(-\frac{17}{2} + \frac{19}{2}Q_x^{(II)} + \frac{5}{2}Q_x^{(II)}Q_y^{(II)}) \times K + Q_x^{(II)}(\frac{1}{2}Q_y^{(II)} + 1) \times C_{FFFT2D}(P_x^{(II)}, P_y^{(II)})^\ddagger$	2D K -input pruned FFT
Total	$(-2 + \frac{3}{2}Q_x^{(I)} + \frac{3}{2}Q_y^{(I)} + \frac{19}{2}Q_x^{(II)} + \frac{5}{2}Q_x^{(II)}Q_y^{(II)})K - M$ $+ (\frac{1}{2}Q_x^{(I)} + 1) \times C_{FFFT1D}(P_x^{(I)}) + (\frac{1}{2}Q_y^{(I)} + 1) \times C_{FFFT1D}(P_y^{(I)})$ $+ Q_x^{(II)}(\frac{1}{2}Q_y^{(II)} + 1) \times C_{FFFT2D}(P_x^{(II)}, P_y^{(II)})$ Operations	

† 1D Split-Radix: $C_{FFFT1D}(N) = 4N \log_2 N - 6N + 8$ ‡ 2D Split-Radix: $C_{FFFT2D}(N_x, N_y) = 4N_x N_y \log_2 N_x N_y - 12N_x N_y + 8N_x + 8N_y$

TABLE II

SUMMARY OF THE COMPUTATIONAL COMPLEXITY OF THE CONTINUOUS AND DISCRETE TRANSFORMS OF A SINGLE RECTILINEAR POLYGON IN TERMS OF THE TOTAL NUMBER OF ADDITIONS AND MULTIPLICATIONS.

Complexity of the Transforms:			
PCHT	$\approx \left(\sum_{i=0}^{M-1} \sum_{j=0}^{J-1} \left\lceil \frac{2^j P_i}{N} \right\rceil (\Lambda_{i\alpha}(K_i) + 26) \right) + M^\dagger$	DHT	$8 \frac{N^2-1}{3}$
	Goertzel	TD-FFT	
FCFS	$((N_x + \frac{1}{4})(N_y + \frac{5}{4}) + \frac{19}{16})K - M$	See Table I	FFT $\frac{1}{2}(4N_x N_y \log_2 N_x N_y - 12N_x N_y + 8N_x + 8N_y)^\ddagger$

$^\dagger \Lambda_{i\alpha}(K_i)$ given in (9) ‡ Row-column real split-radix FFT complexity [24]

Algorithm 1 IntersectionArea(\mathcal{P} , \mathbf{T}_{j,k_x,k_y})

Require: A rectilinear polygon \mathcal{P} . The support \mathbf{T}_{j,k_x,k_y} of the basis function φ_{j,k_x,k_y} .

Ensure: I is the intersection area of \mathcal{P} and \mathbf{T}_{j,k_x,k_y} .

- 1: $I \leftarrow 0$
- 2: $a_1 \leftarrow k_x N_x / 2^j$, $b_1 \leftarrow k_y N_y / 2^j$
- 3: $a_2 \leftarrow (k_x + 1)N_x / 2^j$, $b_2 \leftarrow (k_y + 1)N_y / 2^j$
- 4: **for** every horizontal edge $(x_i, y_i) \rightarrow (x_{i+1}, y_i)$ of \mathcal{P} **do**
- 5: $u \leftarrow \min(x_i, x_{i+1})$, $v \leftarrow \max(x_i, x_{i+1})$
- 6: **if** $a_2 \leq u$ or $v \leq a_1$ or $y_i \leq b_1$ **then**
- 7: continue
- 8: **end if**
- 9: $s \leftarrow \text{sign}(x_{i+1} - x_i)$
- 10: $I \leftarrow I + s(\min(v, a_2) - \max(u, a_1))(\min(y_i, b_2) - b_1)$
- 11: **end for**

Proposition 3: Given a polygon \mathcal{P} with K vertices, its CFS $\hat{F}_{k,l}$, $k, l \in \mathbb{Z}^2$, is given by

$$\hat{F}_{0,0} = \alpha_{0,0} \sum_{i=0}^{K/2-1} y_{2i}(x_{2i+1} - x_{2i}), \quad (11)$$

$$\hat{F}_{k,0} = \alpha_{k,0} \sum_{i=0}^{K/2-1} (y_{2i-1} - y_{2i})e^{-jw_x k x_{2i}}, \quad (12)$$

$$\hat{F}_{0,l} = \alpha_{0,l} \sum_{i=0}^{K/2-1} (x_{2i+1} - x_{2i})e^{-jw_y l y_{2i}}, \quad (13)$$

$$\hat{F}_{k,l} = \alpha_{k,l} \sum_{i=0}^{K/2-1} e^{-jw_y l y_{2i}} (e^{-jw_x k x_{2i+1}} - e^{-jw_x k x_{2i}}), \quad (14)$$

where the scaling factor $\alpha_{k,l}$ is defined as follows

$$\alpha_{k,l} = \begin{cases} \frac{1}{\sqrt{N_x N_y}} & \text{if } k = l = 0 \\ \frac{j}{2\pi k} \sqrt{\frac{N_x}{N_y}} & \text{if } k \neq 0 \text{ and } l = 0 \\ \frac{j}{2\pi l} \sqrt{\frac{N_y}{N_x}} & \text{if } k = 0 \text{ and } l \neq 0 \\ -\frac{\sqrt{N_x N_y}}{4\pi^2 k l} & \text{if } k \neq 0 \text{ and } l \neq 0 \end{cases}$$

It turns out that, except for $\hat{F}_{0,0}$, all coefficients can be computed using DFTs of very sparse signals as we restrict the vertices to lie on the integer lattice. We can decompose the algorithm into four steps, with each step computing one of (11) to (14). For simplicity, we consider only the transform of a single polygon here.

Step 1: Directly compute (11). It is the scaled area of \mathcal{P} . $\hat{F}_{0,0} = \alpha_{0,0} \text{Area}(\mathcal{P})$. This corresponds to line 11 and 18 in the Algorithm 2.

Step 2: Compute (12) as a 1D DFT: $\hat{F}_{k,0} = \alpha_{k,0} \text{DFT}_{k'} \{ \tilde{f}_x \}$, where $k' \equiv k \pmod{N_x}$ and

$$\tilde{f}_x[n] = \sum_{i \in \mathcal{X}_n} (y_{i-1} - y_i), \quad n = 0, \dots, N_x - 1,$$

where $\mathcal{X}_n = \{i \mid x_i \equiv n \pmod{N_x}\}$. The values $(y_{i-1} - y_i)$ are the lengths of the vertical edges. This corresponds to line 5 and 16 in the Algorithm 2.

Step 3: Compute (13) as a 1D DFT: $\hat{F}_{0,l} = \alpha_{0,l} \text{DFT}_{l'} \left\{ \tilde{f}_y \right\}$, where $l' \equiv l \pmod{N_y}$ and

$$\tilde{f}_y[n] = \sum_{i \in \mathcal{Y}_n} (x_{i+1} - x_i), \quad n = 0, \dots, N_y - 1,$$

where $\mathcal{Y}_n = \{i \mid y_i \equiv n \pmod{N_y}\}$. The values $(x_{i+1} - x_i)$ are the lengths of the horizontal edges. This corresponds to line 8 and 17 in the Algorithm 2.

Step 4: Compute (14) as a 2D DFT: $\hat{F}_{k,l} = \alpha_{k,l} \text{DFT}_{k',l'} \left\{ \tilde{f}_{xy} \right\}$, where $k' \equiv k \pmod{N_x}$, $l' \equiv l \pmod{N_y}$ and

$$\tilde{f}_{x,y}[m,n] = \sum_{i=0}^{K/2-1} (\mathbb{1}_{\mathcal{Z}_{m,n}}(x_{2i+1}, y_{2i}) - \mathbb{1}_{\mathcal{Z}_{m,n}}(x_{2i}, y_{2i}))$$

where $\mathcal{Z}_{m,n} = \{(x,y) \mid (x,y) \in \mathbb{Z}^2, x \equiv m \pmod{N_x}, y \equiv n \pmod{N_y}\}$. This is a sparse $N_x \times N_y$ image with 1's and -1's placed at the vertices. This corresponds to line 8, 9 and 15 in the Algorithm 2.

For multiple polygons, we can use (7) for Step 1, and the linearity of the DFT is used to include all the polygons in \tilde{f}_x , \tilde{f}_y and \tilde{f}_{xy} for the three other steps. The four steps are illustrated in Fig. 6. Algorithm 2 gives the pseudocode of FCFS. In practice, it is often possible to combine the creation of \tilde{f}_x , \tilde{f}_y and \tilde{f}_{xy} with the computation of the DFTs, in which case no full-length arrays need to be stored.

Having reduced the problem of computing the CFS to a few real DFTs of sparse signals, we can exploit the extensive collection of available DFT algorithms. The FFT algorithm [25] is not the most efficient in our case, as we could also use a single FFT on a sampled version of f_T , albeit with some loss of precision. If we are only interested in a few CFS coefficients, we can apply a Goertzel-like algorithm [26] to the direct computation of the CFS coefficients using Proposition 3. The pruned FFT is the most appealing approach for the computation of a large number of CFS coefficients, and in particular the transform decomposition FFT (TD-FFT) as it is the fastest of all existing pruned FFT algorithms [27], [28]. The complexity analysis considers both TD-FFT and Goertzel, while the implementation is focused solely on TD-FFT.

2) *Complexity:* As in the Haar case, the computational complexity depends on polygon geometry. In this case, only K , the sum of the number of vertices of the M polygons present in the tile, is important.

We compare in terms of complexity FCFS with the split-radix FFT [24] performed on the discrete image of a polygon. We choose the split-radix FFT algorithm for it is one of the fastest and most widely used FFT algorithms. For FCFS, we consider both Goertzel and TD-FFT algorithms to compute the sparse DFTs.

For the complexity analysis, consider the transform of a $N_x \times N_y$ tile, where N_x and N_y are composite numbers. Table I details the complexity of each step of the FCFS algorithm described in Section III-C1. As observed in [28], we need to choose the TD-FFT sub-FFTs lengths $P_x^{(I)}$, $P_y^{(I)}$, $P_x^{(II)}$ and $P_y^{(II)}$ such that the overall complexity is minimized, with the constraint that they are dividers of N_x and N_y ,

Algorithm 2 FCFS(\mathcal{P}, N_x, N_y, F)

Require: \mathcal{P} contains the lists of the vertices of the M rectangular polygons where $(x_{m,i}, y_{m,i})$ is the i^{th} , out of K_m , vertex of the m^{th} polygon \mathcal{P}_m . For all $m : x_{m,0} \neq x_{m,1}$. The tile size is $N_x \times N_y$. TD-FFT-1D and -2D take as inputs the DFT length and a sparse array whose non-zero entries are stored in V , and their locations in S .

Ensure: F is an $N \times N$ matrix containing the $N \times N$ first Fourier series coefficients of the polygon \mathcal{P} .

```

1:  $n \leftarrow 0$ ;  $A \leftarrow 0$ 
2: for  $m = 0$  to  $M - 1$  do
3:   for  $i = 0$  to  $K_m - 1$  do
4:     if  $x_{m,i} = x_{m,i+1}$  then
5:        $V^K[n] \leftarrow y_{m,i} - y_{m,i+1}$ ;  $S^K[n] \leftarrow x_{m,i}$ 
6:        $n \leftarrow n + 1$ 
7:     else if  $y_{m,i} = y_{m,i+1}$  then
8:        $V^L[n] \leftarrow x_{m,i+1} - x_{m,i}$ ;  $S^L[n] \leftarrow y_{m,i}$ 
9:        $V^{KL}[2n] \leftarrow 1$ ;  $S^{KL}[2n] \leftarrow (x_{m,i+1}, y_{m,i})$ 
10:       $V^{KL}[2n+1] \leftarrow -1$ ;  $S^{KL}[2n+1] \leftarrow (x_{m,i}, y_{m,i})$ 
11:       $A \leftarrow A + y_{m,i}(x_{m,i+1} - x_{m,i})$ 
12:    end if
13:  end for
14: end for
15:  $F[k,l] \leftarrow \alpha_{k,l}$  TD-FFT-2D ( $V^{KL}, S^{KL}, N_x, N_y$ )
16:  $F[k,0] \leftarrow \alpha_{k,0}$  TD-FFT-1D ( $V^K, S^K, N_x$ )
17:  $F[0,l] \leftarrow \alpha_{0,l}$  TD-FFT-1D ( $V^L, S^L, N_y$ )
18:  $F[0,0] \leftarrow \alpha_{0,0}A$ 

```

respectively. There is however no closed-form solution to this problem. In addition, this optimization requires knowledge of the specific FFT algorithm used for the sub-FFTs in TD-FFT, which is impossible with modern libraries such as FFTW. Therefore, the lengths of the sub-FFTs need to be chosen such that the runtime on a given architecture is minimized. This can be done offline, and the optimal lengths stored in a look-up table.

For the sake of analysis, we assume that the split-radix FFT algorithm is used for all FFTs. The complexity of the 2D $N_x \times N_y$ complex split-radix FFT is

$$C_{FFT2D} = 4N_x N_y \log_2 N_x N_y - 12N_x N_y + 8N_x + 8N_y$$

real operations. Real-valued data implies the need for roughly half this number of operations. The Goertzel algorithm requires approximately $O(KN_x N_y)$ real operations for an $N_x \times N_y$ -point real DFT with K non-zero inputs. Our algorithm requires the computation of the area of the polygons (step 1), two length- N DFTs with $K/2$ inputs each (steps 2 and 3) and one 2D length- $N_x \times N_y$ DFT with K inputs (step 4). The exact complexity of FCFS is given in Table I. Table II provides a summary of the computational complexity of all the transforms.

IV. PERFORMANCE EVALUATION OF PCHT AND FCFS

In this section, we first describe how PCHT and FCFS are implemented, and then present results benchmarked on real VLSI layouts, comparing the performance to that of traditional

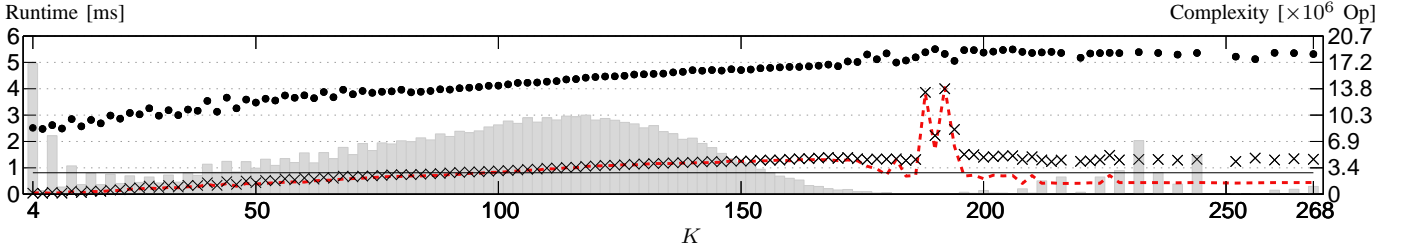


Fig. 8. Median runtime (left y -axis, data points) and complexity (right y -axis, lines) of the PCHT (\times , dashed line) and DHT (\bullet , solid line) of $1024\text{nm} \times 1024\text{nm}$ tiles from the M1 layer containing K vertices. Note the accuracy of our complexity estimate in predicting the qualitative behavior of the PCHT (superposition of crosses and dashed line). Even the outliers around $K = 190$ are predicted. Tiles with $K > 200$ have a lower complexity as they contain only rectangles, which are less complex. However, the complexity is underestimated as it does not take memory transfers into account. The empirical distribution of the number of vertices is shown in gray.

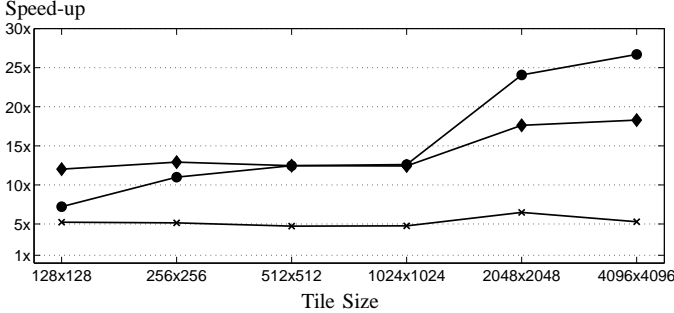


Fig. 9. Speed-up of the average runtime provided by the PCHT on layers M1 (\times), M2 (\blacklozenge), CA (\bullet). The higher the better. 1 times speed-up means same performance as the DHT. We see that PCHT is at least 5 times faster than the DHT. Confidence intervals have been omitted in this figure as in the worst case they were found to be within ± 0.06 of the value given, with 95% confidence.

discrete transform algorithms. This performance evaluation has two goals. The first is to validate the theoretical computational complexity and analyze the behavior of the runtime as a function of the number of vertices K in a tile. The second goal is to measure the improvement in runtime provided by the PCHT and FCFS over the DHT and FFT, respectively.

A. Implementation and Setup of the Benchmark

All algorithms were implemented in a computational lithography tool, and run on a 3GHz Intel $\text{\textcircled{C}}$ Xeon 5450 running Linux $\text{\textcircled{C}}$ in 64-bit mode. All code is C++, single-threaded and was compiled using GCC 4.1.2 with option “-O3”. The tool takes a layout file as input, parses it, chops polygons and places them in their corresponding tiles. Each tile is then transformed individually. Fig. 6 shows flow diagrams of the different steps involved in the process of transforming a layout using PCHT, DHT, FCFS and FFT. The transform is initially performed twice to get the machine into steady state, and then repeated 10 more times to average out the timing noise. Both PCHT and DHT, as described in Section III-B1, were fully custom-implemented. The FFT was performed using the FFTW3 library [29]. FCFS was custom-implemented using the TD-FFT algorithm for pruned FFTs, which in turn use FFTW3 for the sub-FFT. For the discrete transforms, an image of the tile is first created and then fed to the transform algorithm. The time needed to create the discrete image is added to the runtime of the discrete transform.

For the evaluation, the algorithms were run on three layers from a 22nm layout of modest size ($0.43\text{mm} \times 0.33\text{mm}$)

containing rectangles and more complex rectilinear polygons. These layers are M1 and M2, which contain both rectangles and other polygons, and CA, which contains only rectangles, as shown in Fig. 2. We ran the experiment on squared tiles, where side lengths were powers of two from $128\text{nm} \times 128\text{nm}$ to $4096\text{nm} \times 4096\text{nm}$.

This experiment has two distinct goals. The first is to validate the theoretical complexity derived in Section III as a predictor of the behavior of the runtime of the transforms. To that effect, we use the runtime from M1 tiled in $1024\text{nm} \times 1024\text{nm}$. We compute the average of the 10 runs for each tile and for all transforms. We then take the median of this average over all tiles containing a given number of vertices K . This is shown in Fig. 8 and Fig. 10. We plot K on the x -axis, the median runtime on the left y -axis, and the complexity on the right y -axis. The plot also shows in light gray the empirical distribution of K to indicate which range of K is the most important one.

The second is to measure relative difference of runtime between PCHT and FCFS, and their respective discrete counterparts. To that effect, we aggregate the results to get the average of 10 runtimes over a full layer, for all layers and all transforms. Our metric is the speed-up, computed by dividing the average runtime of the discrete transform by the average runtime of the corresponding continuous transform for a given layer and tile size. This is shown in Fig. 9 and Fig. 11. We plot the speed-up of the average runtime for all layers and tile sizes considered.

B. Benchmark Results

Fig. 8 shows the runtime and the complexity of the PCHT and the DHT as a function of K for $1024\text{nm} \times 1024\text{nm}$ tiles from M1. The left and right y -axis show the runtime and complexity, respectively. We observe that the complexity given by (10) describes the qualitative behavior of the runtime of the PCHT very well, even for the outliers around $K = 190$. When $K > 200$ and the tiles are composed exclusively of rectangles, (10) underestimates the complexity. In this case, the runtime is dominated by memory transfers.

The gap between the runtime of the DHT and its complexity is also explained by the domination of memory transfers, which are not accounted for in the computational complexity in (10). The dependence of the DHT on K stems from discrete image creation and from the fact that our implementation uses

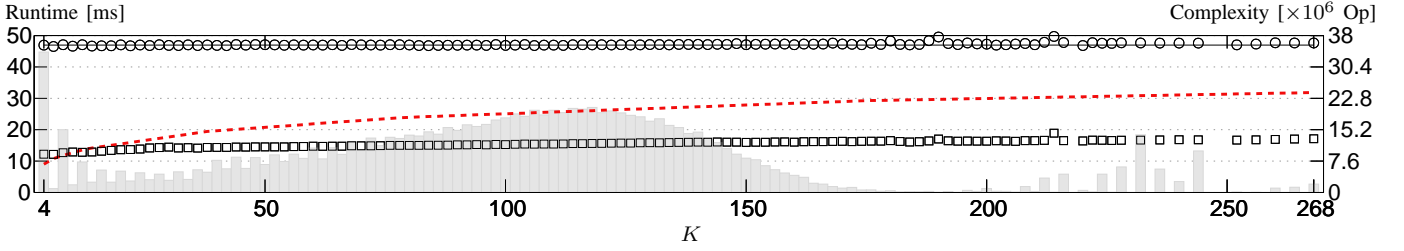


Fig. 10. Median runtime (left y -axis, data points) and complexity (right y -axis, lines) of the FCFS (\square , dashed line) and FFT (\circ , solid line) of $1024\text{nm} \times 1024\text{nm}$ tiles of the M1 layer containing K vertices. We observe that the gap between the runtimes of the FCFS and the FFT is larger than that of their respective complexities. The reason being that the pruned FFT can be implemented more efficiently than the FFT as shown in [30].

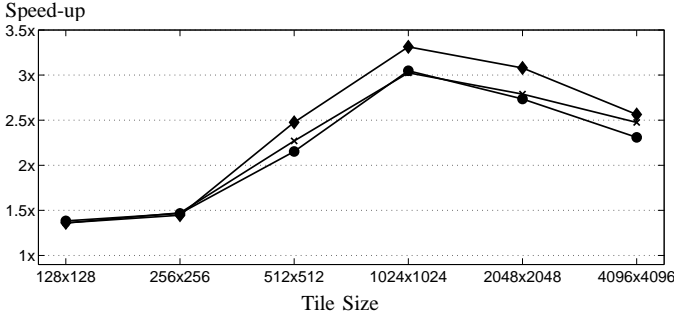


Fig. 11. Speed-up of the average runtime provided by the FCFS on layers M1 (\times), M2 (\blacklozenge), CA (\bullet). The higher the better. 1 times speed-up means same performance as the FFT. We see that PCHT is at least 1.4 times faster than the FFT. Confidence intervals have been omitted in this figure as in the worst case they were found to be within ± 0.012 of the value given, with 95% confidence.

an *if* statement to avoid storing zero transform coefficients whose number decreases with increasing K . Given the very high number of zero coefficients, the cost of the *if* statement is justified by the large memory transfer savings. Overall, this figure shows that for small values of K encountered in VLSI layouts, the PCHT is significantly faster than the DHT.

Fig. 9 shows that the average runtime of the PCHT for a full M1 layer is about 5 times shorter than that of the DHT, for all considered tile sizes. For the CA layer, which contains only rectangles that have a lower complexity, the speed-up is 25 fold for large tiles.

Fig. 10 shows the runtime and the complexity of FCFS and the FFT as a function of K for $1024\text{nm} \times 1024\text{nm}$ tiles from M1. The left and right y -axis show the runtime and complexity, respectively. The runtime of FCFS compared with that of the FFT is lower than expected given the theoretical complexity. Indeed, as shown by Franchetti and Püschel [30], the pruned FFT can be implemented more efficiently than the FFT. Here again, the FCFS is significantly faster than the FFT for small values of K found in VLSI layouts.

The speed-up achieved by FCFS over the FFT, shown in Fig. 11, is similar for all considered layers. The M2 layer shows a slightly higher speed-up because its vertex density is lower than that of other layers. For all layers, the highest speed-up found is for $1024\text{nm} \times 1024\text{nm}$ tiles, for which the FCFS is about 3 times faster than the FFT. In contrast, the results for $128\text{nm} \times 128\text{nm}$ and $256\text{nm} \times 256\text{nm}$ show only a modest speed-up of about 1.5.

For all speed-up results, confidence intervals were computed at the 95% level but found to be negligible and have thus been

TABLE III
AVERAGE RUNTIME OF THE TRANSFORMS OF AN M1 LAYER DIVIDED INTO $1024\text{nm} \times 1024\text{nm}$ TILES. THERE ARE 127544 NON-EMPTY TILES FOR A TOTAL OF 995497 RECTANGLES AND 428817 OTHER POLYGONS. RUNTIME PER TILE IS IN μ -SECONDS. TOTAL RUNTIME IS IN SECONDS.

Average runtime (with 95% confidence intervals)				
	PCHT	DHT	FCFS	FFT
Per Tile [μ s]	919 ± 0.6	4375 ± 12.8	15648 ± 10	47341 ± 8
Total [s]	117.2 ± 0.2	558 ± 4.5	1996 ± 4	6038 ± 3

omitted in the figures. However, they can be found in Table III, which contains average runtime values of all considered transforms, for the M1 layer divided into $1024\text{nm} \times 1024\text{nm}$ tiles, both per tile and for the whole layer. For the 127544 tiles of M1, the runtime is found to be on average about 5 times lower for the PCHT and 3 times lower for the FCFS, respectively, than for their discrete counterparts. Although these numbers might at first glance seem modest, the runtime is reduced from about 9min for the DHT to only 2 using PCHT, whereas the FCFS runs in 30min instead of 1h40min for the FFT. These are significant time savings.

V. CONCLUSIONS AND FUTURE WORK

We developed PCHT and FCFS, two new fast algorithms for the computation of the continuous Haar transform and continuous Fourier series, respectively, of patterns of rectilinear polygons, as are typically found in VLSI layouts. We showed that the sparsity of the polygon description can indeed be exploited by continuous transforms, resulting in significant speed-up of the transform coefficients computation. The complexities of the two algorithms were analyzed and compared with that of their discrete counterparts. They were found to be lower in complexity when the number of vertices of the polygons is low, as is the case in VLSI layouts. We validated this analysis by implementing all algorithms in a computational lithography software and running a performance evaluation on VLSI layouts. The results not only confirmed the validity of our complexity analysis, but also showed that continuous transforms can actually be implemented more efficiently than their discrete counterparts. This is achieved thanks to a more compact description of the input signal, allowing a better usage of the available cache and reducing memory transfers. We measured the gain in performance using a speed-up metric. PCHT was found to run at least 5 times

faster than the DHT for all considered layers and tile sizes. A maximum speed-up of 30 times was achieved in the case of the CA layer divided in $4096\text{nm} \times 4096\text{nm}$ tiles. FCFS showed least improvement for small tiles size where it is only 1.5 times faster than the FFT. However, it showed a peak performance for $1024\text{nm} \times 1024\text{nm}$ tiles where it is over 3 times faster than the FFT. These speed-ups result in significant time savings due to the magnitude of the problem at hand. We therefore conclude that the PCHT and FCFS are superior to the DHT and FFT, respectively, for rectilinear polygons in VLSI layouts.

In lithography, often only low-pass Fourier coefficients are needed, and it would be of high interest to adapt FCFS to yield only this low-pass spectrum. For the sake of speed, it is currently common practice to employ decimation using a crude low-pass filter, such as a Haar scaling function, followed by an FFT, accepting the inevitable large imprecision. Straightforward adaptation of FCFS using input and output pruned FFT, or even Goertzel, to yield only the low-pass unaliased spectrum does not compete in terms of speed with the aforementioned decimation scheme. More sophisticated spectral methods need thus to be investigated to find a suitable trade-off between speed and accuracy.

We designed PCHT and FCFS with highly suitable structures for parallelization. Given the trend towards multi- and manycore architectures, such a parallel implementation would be a natural next step. Given the close relationship between the Fourier and cosine transforms, straightforward extension of the FCFS algorithm to the continuous cosine series is possible. A further research avenue would be to apply continuous transforms to other application domains. For example, relaxing the signal model to non-rectilinear polygons or even radically different sparse parametric signals.

ACKNOWLEDGMENT

The authors thank Markus Püschel for providing useful advice on the FFT and pruned FFT.

REFERENCES

- [1] G. E. Moore, "Cramming more components onto integrated circuits," *Electronics*, vol. 38, no. 8, pp. 114–117, Apr. 1965.
- [2] C. Mack, *Fundamental Principles of Optical Lithography: The Science of Microfabrication*. Wiley, Jan. 2008.
- [3] J. W. Goodman, *Introduction to Fourier Optics*, 3rd ed. Roberts & Company Publishers, Dec. 2004.
- [4] A. K.-K. Wong, *Resolution Enhancement Techniques in Optical Lithography*. Bellingham, WA USA: SPIE Press, 2001.
- [5] F. M. Schellenberg and B. W. Smith, "Resolution enhancement technology: The past, the present, and extensions for the future," in *Proc. SPIE*, vol. 5377, May 2004, pp. 1–20.
- [6] R. H. Stulen and D. W. Sweeney, "Extreme ultraviolet lithography," *IEEE J. Quantum Electron.*, vol. 35, no. 5, pp. 694–699, May 1999.
- [7] A. E. Rosenbluth, S. J. Bukofsky, M. S. Hibbs, K. Lai, A. F. Molless, R. N. Singh, A. K. K. Wong, and C. J. Proglar, "Optimum mask and source patterns to print a given shape," in *Proc. SPIE*, vol. 4346, Sep. 2001, pp. 486–502.
- [8] A. Poonawala, P. Milanfar, and D. G. Flagello, "OPC and PSM design using inverse lithography: A nonlinear optimization approach," in *Proc. SPIE*, vol. 6154, Mar. 2006, p. 61543H.
- [9] K. Kryszczuk, P. Hurley, and R. Sayah, "Direct printability prediction in VLSI using features from orthogonal transforms," in *Proc. of the IAPR International Conference on Pattern Recognition*, Aug. 2010.
- [10] International Technology Roadmap for Semiconductors, "2007 edition," http://www.itrs.net/Links/2007ITRS/2007_Chapters/2007_Lithography.pdf, 2007.
- [11] M. E. Haslam, J. F. McDonald, D. C. King, M. Bourgeois, D. G. L. Chow, and A. J. Steckl, "Two-dimensional Haar thinning for data base compaction in Fourier proximity correction for electron beam lithography," *J. Vac. Sci. Technol., B: Microelectronics and Nanometer Structures*, vol. 3, no. 1, pp. 165–173, Jan. 1985.
- [12] X. Ma and G. R. Arce, "Generalized inverse lithography methods for phase-shifting mask design," *Opt. Express*, vol. 15, no. 23, pp. 15 066–15 079, Nov. 2007.
- [13] J. Antoine, R. Murenzi, P. Vandergheynst, and S. T. Ali, *Two-Dimensional Wavelets and their Relatives*. Cambridge University Press, 2004.
- [14] R. Scheibler, P. Hurley, and A. Chebira, "Pruned continuous Haar transform of 2D polygonal patterns with application to VLSI layouts," to appear in: *The Int. Cong. on Computer Applications and Computational Science*, 2010.
- [15] D. G. L. Chow, J. F. McDonald, D. C. King, W. Smith, K. Molnar, and A. J. Steckl, "An image processing approach to fast, efficient proximity correction for electron beam lithography," *J. Vac. Sci. Technol., B: Microelectronics and Nanometer Structures*, vol. 1, pp. 1383–1390, Oct. 1983.
- [16] J. F. Chen, H. Liu, T. Laidig, C. Zuniga, Y. Cao, and R. Socha, "Development of a computational lithography roadmap," in *Proc. SPIE*, vol. 6924, 2008, p. 69241C.
- [17] S. W. Lee and R. Mittra, "Fourier transform of a polygonal shape function and its application in electromagnetics," *IEEE Trans. Antennas Propag.*, vol. 31, no. 1, pp. 99–103, 1983.
- [18] F. L. Chu and C. F. Huang, "On the calculation of the Fourier transform of a polygonal shape function," *J. of Physics A: Math. and General*, vol. 22, pp. L671–L672, 1989.
- [19] L. Brandolini, L. Colzani, and G. Travaglini, "Average decay of Fourier transforms and integer points in polyhedra," *Ark. Mat.*, vol. 35, no. 2, pp. 253–275, 1997.
- [20] Y. M. Lu, M. N. Do, and R. S. Laugesen, "A computable Fourier condition generating alias-free sampling lattices," *IEEE Trans. Signal Process.*, vol. 57, no. 5, pp. 1768–1782, 2009.
- [21] M. Vetterli, J. Kovačević, and V. K. Goyal, "The world of Fourier and wavelets: Theory, algorithms and applications," <http://www.fourierandwavelets.org/>, 2009.
- [22] S. Mallat, *A Wavelet Tour of Signal Processing: The Sparse Way*, 3rd ed. Academic Press, Dec. 2008.
- [23] N. U. Ahmed and K. R. Rao, *Orthogonal Transforms for Digital Signal Processing*. Springer-Verlag New York, Inc., 1975.
- [24] P. Duhamel and H. Hollmann, "Split radix FFT algorithm," *Electron. Lett.*, vol. 20, no. 1, pp. 14–16, 1984.
- [25] J. W. Cooley and J. W. Tukey, "An algorithm for the machine calculation of complex Fourier series," *Math. Comput.*, vol. 19, no. 90, pp. 297–301, 1965.
- [26] G. Goertzel, "An algorithm for the evaluation of finite trigonometric series," *The American Mathematical Monthly*, vol. 65, no. 1, pp. 34–35, Jan. 1958.
- [27] H. Sorensen and C. Burrus, "Efficient computation of the DFT with only a subset of input or output points," *IEEE Trans. Signal Process.*, vol. 41, no. 3, pp. 1184–1200, 1993.
- [28] M. Medina-Melendrez, M. Arias-Estrada, and A. Castro, "Input and/or output pruning of composite length FFTs using a DIF-DIT transform decomposition," *IEEE Trans. Signal Process.*, vol. 57, no. 10, pp. 4124–4128, 2009.
- [29] M. Frigo and S. Johnson, "The design and implementation of FFTW3," *Proc. IEEE*, vol. 93, no. 2, pp. 216–231, 2005.
- [30] F. Franchetti and M. Püschel, "Generating high performance pruned FFT implementations," in *IEEE Int. Conf. on Acoustics, Speech and Signal Processing*, pp. 549–552, 2009.